ORIGINAL RESEARCH ARTICLE

Effect of NbC Addition on the Microstructure and Wear Resistance of Laser Cladding Nickel-Based Alloy Coatings

Yingpeng Liu, Kaiming Wang, Hanguang Fu, Xiaojun Yang, and Jian Lin

Laser cladding nickel-based alloy coating has dense microstructure and good bonding with base material, but its wear resistance is difficult to meet the requirements of harsh environment. In order to enhance the microhardness and wear resistance of nickel-based coatings, NbC ($0.6 < d < 5$ μm) was added directly to Ni45 powder to prepare laser cladding nickel-based composite coatings. By studying the microstructure, microhardness and wear resistance, it was found that the main phases in the coating were γ-Ni solid solution and precipitated phases such as $Cr_{23}C_6$, Cr_7C_3 and NbC. The addition of NbC inhibits the formation of $Cr_{23}C_6$ and the total carbide content within the coating is reduced, which limited the further improvement of the microhardness of the coating. Due to the refining effect of Nb, the dendrite arm spacing was reduced up to 64.7% of the 1# coating, and the grain size was reduced to 60.0% of the 1# coating, and the coatings demonstrate better wear resistance during frictional wear.

1. Introduction

The application of high-strength steels in the manufacture of automobile bodies has been an important way to achieve the lightweight of automobiles, but it has also led to greater impact loads on the molds, thus aggravating the wear of the mold (Ref 1-3). The worn mold can be repaired by laser cladding, additive manufacturing, surfacing, spraying and other technologies, which can reduce the replacement frequency of the mold (Ref 4-7). Among them, laser cladding, as a new surface strengthening and repair technology, has been widely used in equipment repair of automobiles, mining machinery, aerospace and other fields by its advantages of small heat-affected zone, rapid solidification and low heat input (Ref 8-11). Laser cladding nickel-based coating has a dense microstructure, high bonding strength with the base material and excellent oxidation resistance (Ref 12, 13). Nickel-based composite coating with higher hardness and wear resistance is often prepared by adding WC, TiC, NbC, B_4C and other hard ceramic phases (Ref 14-17).

The direct addition method is a method of preparing a composite coating by adding ceramic powder directly into the cladding powder. It has the advantages of simple and fast

operation (Ref 18, 19). NbC has high hardness, and its density is 7.79 g/cm^3, which is very close to the density of nickel-based alloy. Uniformly distributed NbC phase with high hardness and the refining effect of Nb element on microstructure contributed to the enhancement of the wear resistance of coatings. Many scholars have done a lot of research on this (Ref 20, 21). Li et al. added micro–nano-NbC powder to the high-entropy alloy powder, and it was observed under transmission electron microscopy that nanoscale NbC partially dissolved and re-precipitated in the laser cladding process (Ref 22). The nailing effect of NbC on dislocation was observed under TEM, which improved the mechanical properties of the material. Chen et al. added NbC into the Fe-based powder, and the study showed that the prepared composite coating had fine grains, NbC was evenly distributed at the grain boundary, and the microhardness and wear resistance of the coating were effectively boosted (Ref 23). Wang et al. added B_4C and pure niobium powder to the Fe-based powder to prepare the Fe-based composite coating. The microstructure of the coating was significantly refined, the NbC phase was detected in the coating, and the wear resistance of the coatings were substantially increased (Ref 24). Cao et al. prepared the Fe-based coating by adding NbC by mechanical addition method (Ref 25). It was observed that NbC decomposed and re-precipitated during the laser cladding process. A slight increase in the microhardness of the coatings was observed, but the enhancement of the wear resistance was more pronounced.

In our previous study, NbC was synthesized in situ using FeNb65 and Cr_3C_2 to prepare nickel-based composite coatings (Ref 26). The preparation process was complicated, and the generated hard ceramic phase had large particles. Fluctuations in friction coefficient and wear resistance were caused by the exfoliation of the hard phase with large particles during frictional wear. Therefore, the preparation of Ni45-NbC composite coatings by direct addition method attracted our attention. In this paper, from the perspective of preparing coatings with stable wear resistance and enriching the hard phase addition process, the effect of direct addition of different

Yingpeng Liu, Hanguang Fu, Xiaojun Yang, and **Jian Lin**, Key Laboratory of Advanced Functional Materials, Ministry of Education, Department of Materials Science and Engineering, Beijing University of Technology, Number 100, Pingle Garden, Chaoyang District, Beijing 100124, People's Republic of China; and **Kaiming Wang**, College of Automobile and Mechanical Engineering, Changsha University of Science and Technology, Changsha, People's Republic of China. Contact e-mail: hgfu@bjut.edu.cn.

amounts of microscale and nanoscale particle size NbC on the properties of nickel-based coatings was evaluated. The analysis focuses on the microstructural characteristics, hardness and wear properties of the coatings so that it can provide guidance for engineering applications.

2. Materials and Methods

2.1 Materials

The substrate used in the test is Cr12MoV die steel (12 mm × 60 mm × 100 mm), which is the most commonly used die steel in the automotive manufacturing industry. Before laser cladding, the rust on the substrate surface is removed by polishing with an Angle grinder, and then, the surface dirt and oil are removed by cleaning with ethanol. In this experiment, Ni45, which has excellent wear resistance and low price, was selected as the matrix material for the laser cladding experiment. Nickel-based composite coating powders consist of Ni45 and NbC. Ni45 powder is a standard spherical powder with a particle size of 45-105 μm, and the powder morphology is shown in Fig. 1(a). The particle size distribution was counted using image software, and the results are shown in Fig. 1(c), with an average particle size of 71.82 μm. NbC powder is an

irregular powder with particle size ranging from 0.5 to 6 μm, and the powder shape is shown in Fig. 1(b). The particle size distribution was counted using image software, and the results are shown in Fig. 1(d), with an average particle size of 1.89 μm. Both Ni45 and NbC were purchased from Beijing Xingrongyuan Technology Co., Ltd. In order to study the effect of NbC addition on the microstructure and wear resistance of nickel-based alloy coating, the above two powders were evenly mixed according to the designed content of Ni45-xNbC (x = 0, 5, 10, 15, 20, 25 wt.%) and then dried in a dryer at 75 °C for 2 h for reserve. The composition of the test substrate Cr12MoV and Ni45 powder is shown in Table 1, and the coating number and composition design are shown in Table 2.

2.2 Laser Cladding Parameters

In the test, the YLS-6000-S2 fiber laser made by IPG Company was used, and the covering head of a six-axis linkage robot made by ABB company was used to control the powder in the way of coaxial powder feeding. The laser produces a continuous laser with a wavelength of 1070 nm and a maximum power of 6.0 kW. The optical system produces a square spot with a size of 5 mm × 5 mm on the surface of the substrate. The coatings were prepared on the surface of Cr12MoV, and 15L/min argon gas was applied to protect the molten pool from oxidation during laser cladding. A single
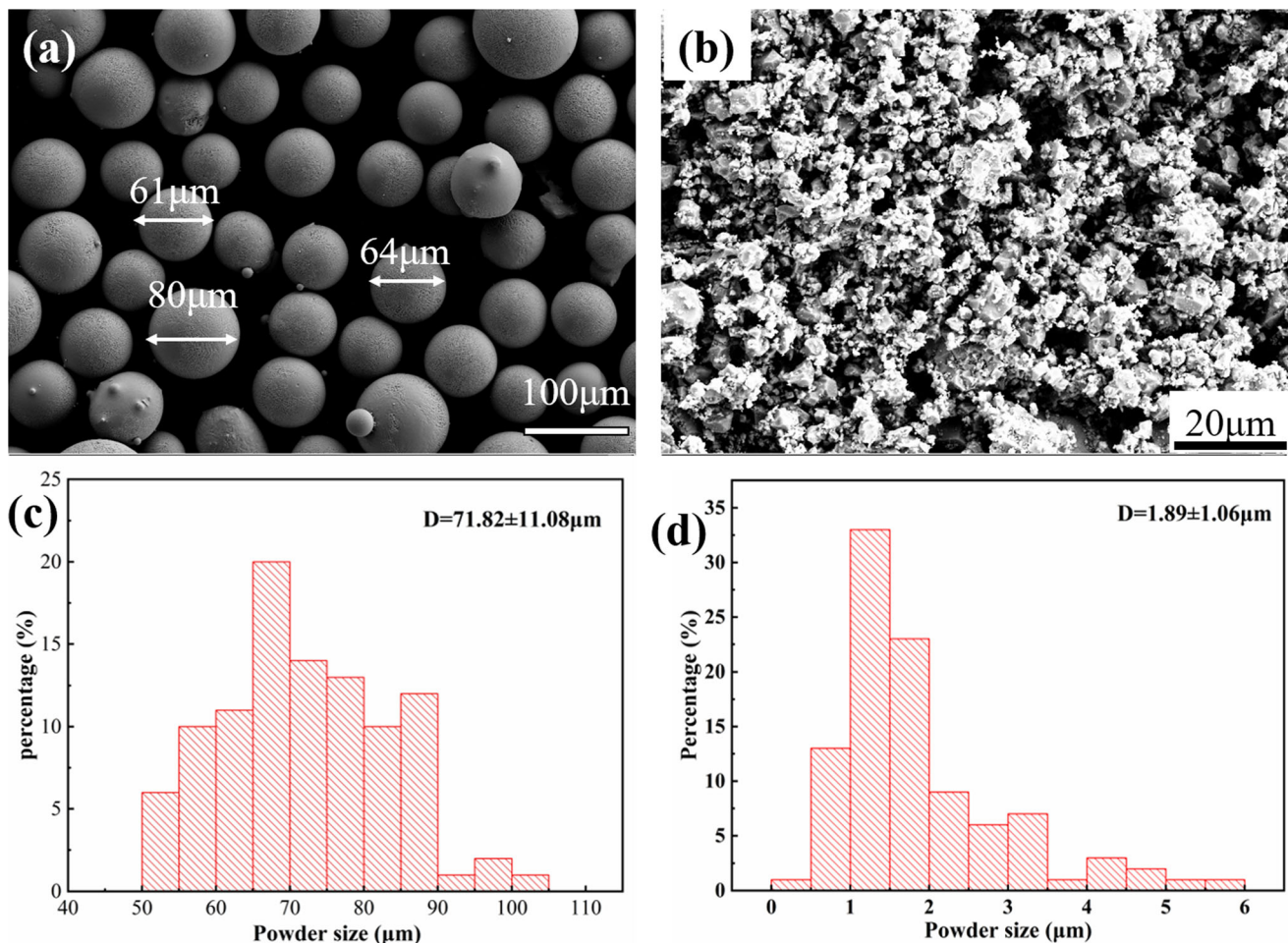

Fig. 1 SEM images of laser cladding powder: (a) Ni45; (b) NbC; (c) particle size distribution of Ni45 powder; (d) particle size distribution of NbC powder

Table 1　Chemical composition of Ni45 powders and Cr12MoV steel (wt.%)

	Fe	Ni	Cr	B	Si	C	Mn	P	V	Mo	S	Cu
Ni45	5.30	Bal.	10.02	1.89	3.05	0.33	…	…	…	…	…	…
Cr12MoV	Bal.	0.11	12.30	…	0.27	1.45	0.21	0.02	0.27	0.55	0.01	0.13

Table 2　Coating number and chemical composition design (wt.%)

No.	1#	2#	3#	4#	5#	6#
Ni45	100	95	90	85	80	75
NbC	0	5	10	15	20	25

Table 3　Summary of laser cladding parameters

Feature	Description
Laser power, kw	2.0
Powder feed rate, g min^{-1}	15
Travel speed, mm s^{-1}	4
Laser shield gas flow, L min^{-1}—argon	15
Overlap rate, %	35

bead and six beads are cladding to the surface of the substrate, and all coatings are cladding in three layers. The process parameters of laser cladding are shown in Table 3.

2.3 Observation of Microstructure

The metallographic samples were cut from the single bead coatings along the direction perpendicular to the coating, then machined with 240 mesh, 500 mesh, 1200 mesh and 2000 mesh SiC sandpaper on the polishing machine and then polished with diamond polishing (W2.5) paste. After polishing the samples, they were etched with aqua regia (HNO$_3$: HCl = 1:3) for 15 s. The polished samples used for electron backscatter diffraction (EBSD) were finally vibro-polished with a 0.02 μm silica suspension for 40 min, and the polishing load is 50%. The microstructure and morphology of the coatings were observed and analyzed by scanning electron microscopy (ZEISS Gemini SEM 300), and the elements were observed by energy-dispersive spectrometer (EDS). Grain size and residual stress were evaluated by electron backscattering diffraction (EBSD Zeiss, Germany). In addition, the area share of carbides and the morphology of NbC were counted using image processing software. Samples of 19 mm × 12 mm × 12 mm were cut on the surface of coatings in the direction perpendicular to the coating. After mechanical grinding with 240 mesh SiC sandpaper, Cu-Kα radiation x-ray diffractometer (BRUKER D8 Advance) was used to characterize the crystal structure of the phase. Specific parameters were as follows: tube voltage 40 kV, tube current 40 mA, scanning speed 8°/min, scanning range 20°-90° coupled continuous scanning and step length 0.02°.

2.4 Microhardness and Wear Resistance

The microhardness tester (MICRO-MET-5103) was used to measure the microhardness of the sample. The specific parameters were as follows: The test load was 1.96 N, the dwell time was 10 s, 15 points were taken from different areas of the coating surface, and the average value was taken as the average microhardness of the coating surface after removing the maximum and minimum values. The size of the wear sample is 12 mm × 12 mm × 19 mm. High-speed ring friction and wear testing device (Jnstart MRH-3W) was used to carry out the wear test. The grinding ring was GCr15 steel with a hardness of 60 HRC and a speed of 200 r/min. According to the working conditions of die steel in different production environments, 98 N and 196 N were used for friction and wear test of the samples for 2 h. Before and after the friction and wear test, the samples were cleaned by ultrasonic wave with alcohol and weighed by a balance with an accuracy of 0.1 mg. The wear loss weight per unit time of the coating is the wear rate, and the reciprocal of the wear rate is used to represent the wear resistance of the coating. The morphology and roughness of the worn surface were observed and analyzed by laser confocal microscope (OLS40-CB) and scanning electron microscope.

3. Results and Discussions

3.1 Microstructure Analysis

The macroscopic morphologies of laser cladding nickel-based composite coatings are shown in Fig. 2, from which it can be seen that the coating is well formed. Figure 3 shows the morphology of the bottom of the coatings under the optical microscope, and the grains are all dendritic. It could be seen that with the increase in the NbC design content, there is a refining effect on the grains. The dendrite arm spacing (DAS) was measured using Image Pro software, and the test area is the area selected by the red line in Fig. 3, and the test results are summarized in Table 4. Figure 4 shows the metallographic photo of the joint of the coating with the base material under the SEM and the result of linear scanning element analysis at the joint. The white hard phase can be seen evenly distributed throughout the coating. The heat loss at the interface is mainly through the heat conduction of the base material, and the crystal growth direction is opposite to the heat dissipation direction. Therefore, the coating structure near the interface is dendritic. The element Ni is present in high amounts in the coating but rarely in the substrate, and Cr is present in large amounts in the substrate but rarely in the coating. As shown in Fig. 4, Ni and Fe exhibit obvious element diffusion at the interface, indicating that the coating is well combined with the base material (Ref 27-30).

Figure 5 shows the XRD diffraction pattern of laser clad nickel-based alloy coatings with different NbC additions. By comparing the standard diffraction cards and analyzing Jade software, it can be seen that the three main diffraction peaks are
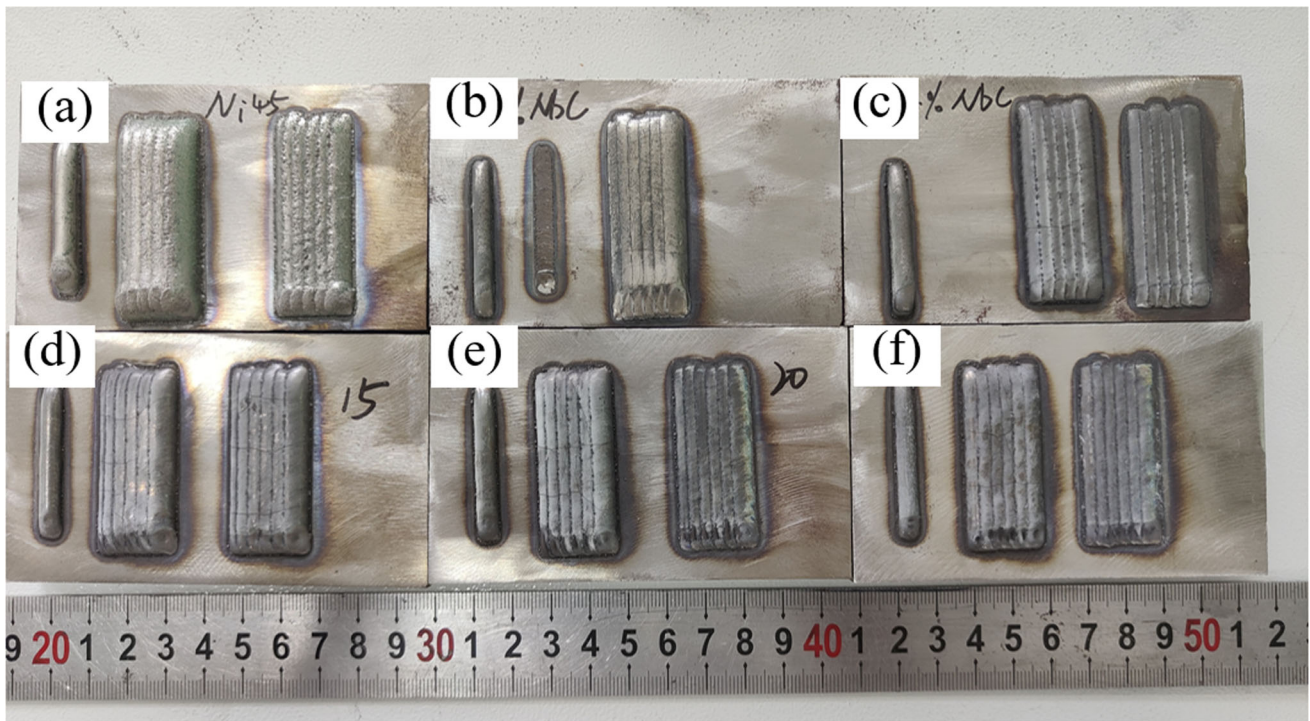
Fig. 2 Macroscopic morphology of nickel-based composite coatings: (a) 1#; (b) 2#; (c) 3#; (d) 4#; (e) 5#; (f) 6#
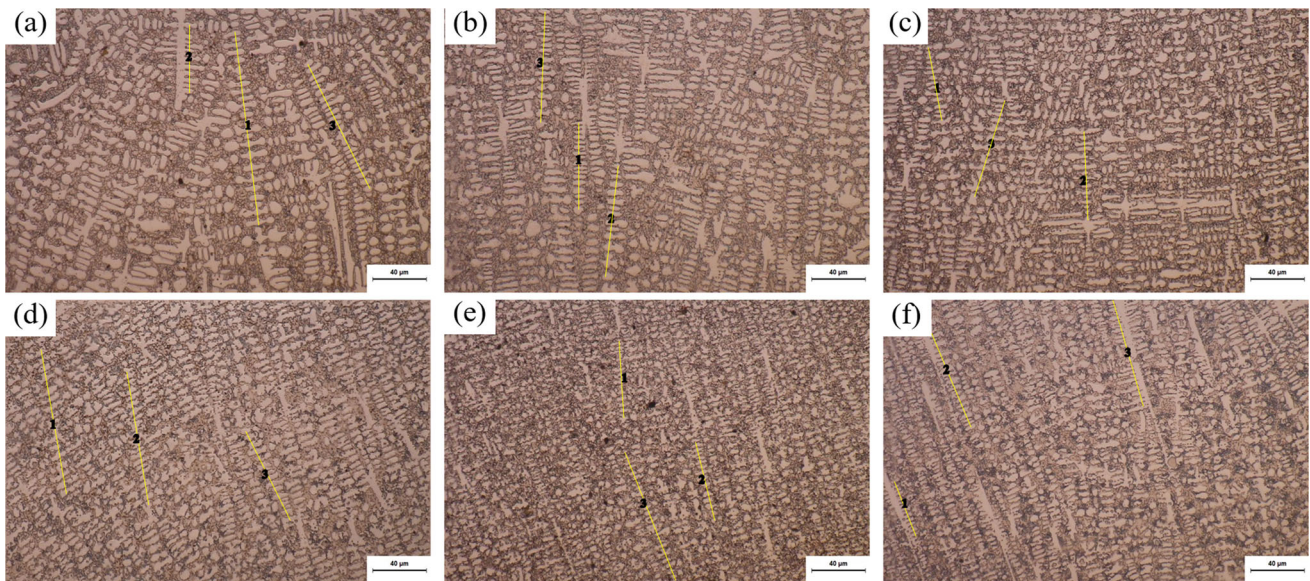

Fig. 3 Microscopic morphology of the bottom of the coatings under the optical microscope: (a) 1#; (b) 2#; (c) 3#; (d)4#; (e) 5#; (f) 6#

Table 4 Results of dendrite arm spacing measurements of coatings

	1#	2#	3#	4#	5#	6#
Total number of DAS	59	46	43	54	52	69
Total DAS, μm	300.2	225.1	192.1	281.9	218.6	225.7
Average DAS, μm	5.1	4.9	4.5	5.2	4.2	3.3

γ-Ni and $Cr_{23}C_6$, and several lower diffraction peaks may represent Cr_7C_3, Cr_2B and NbC. This indicates that the substrate of the coating is mainly composed of γ-Ni solid solution and precipitated phase formed by C, Cr and B. In the five groups of coatings with NbC addition, the NbC diffraction peaks in the diffraction pattern of 2# are not obvious, while the other four groups of coatings have obvious NbC diffraction peaks near 35°, 41° and 58°. With the increase in the addition of NbC, the diffraction peaks of NbC in the diffraction pattern is gradually enhanced, while the intensity of $Cr_{23}C_6$ and Cr_7C_3 diffraction peaks is gradually weakened. This is because Nb is a
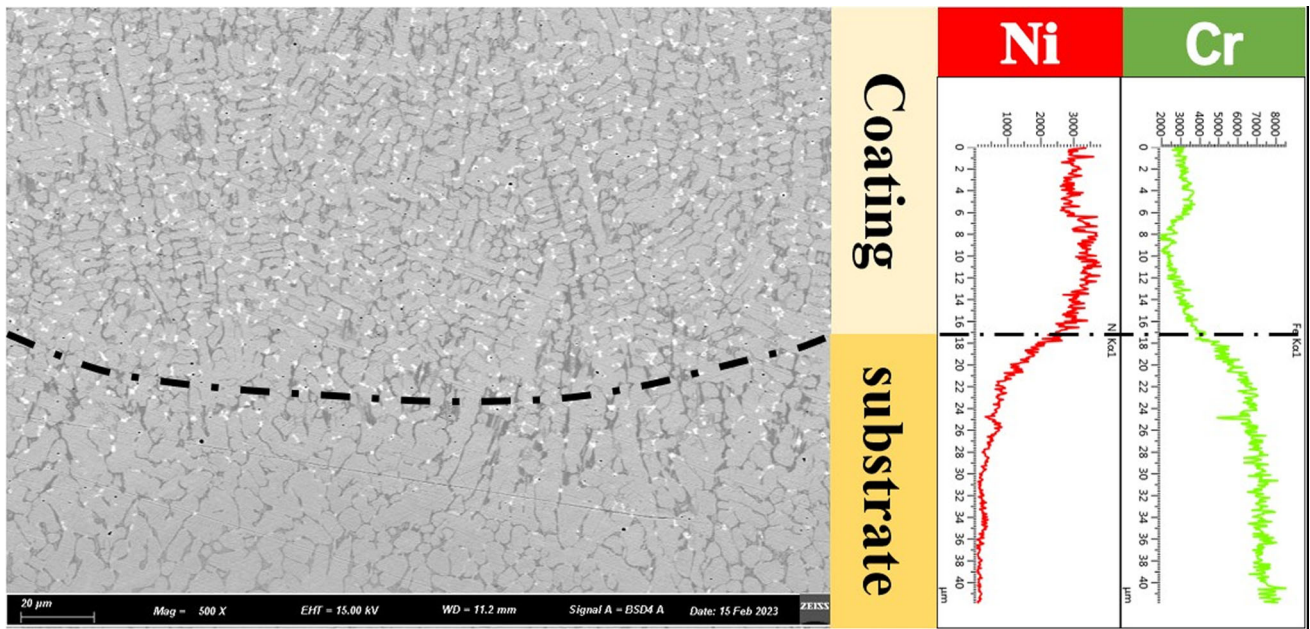
Fig. 4 Morphology of the interface of coating and Cr12MoV and the elemental distribution of the interface
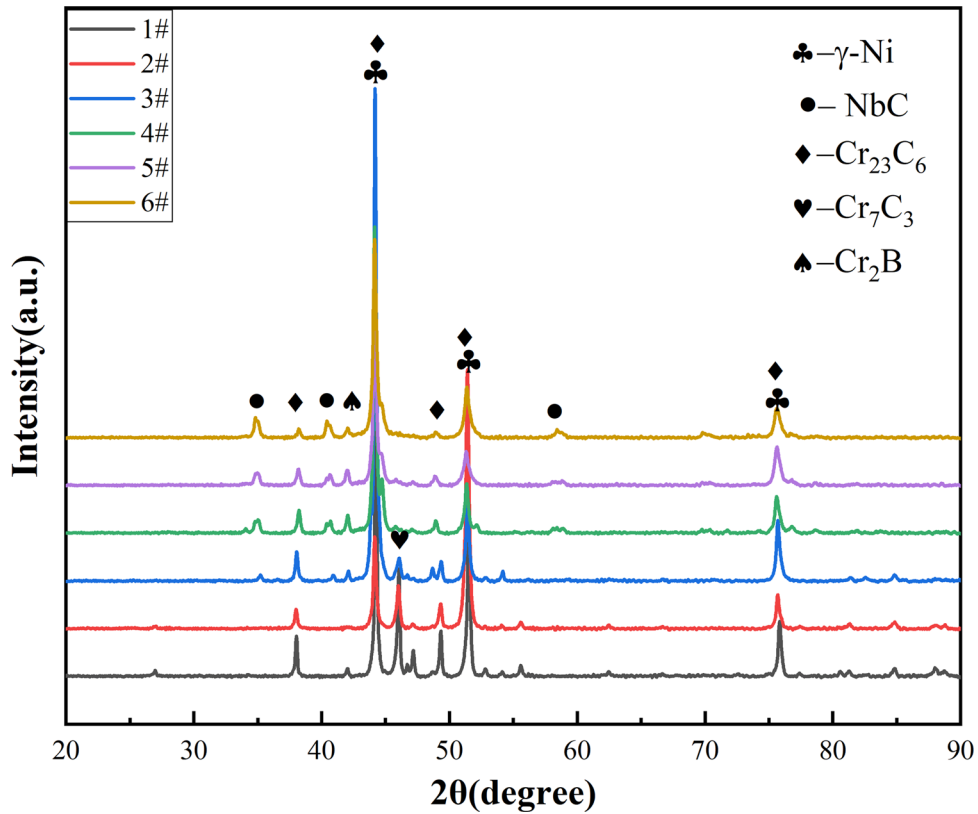

Fig. 5 XRD patterns of laser clad nickel-based alloy coatings with different NbC additions

strong carbide element compared with Cr and has a stronger binding ability with C. Under the high-temperature action of laser cladding, a large amount of element C in the molten pool is burned (Ref 31), and NbC precipitation is preferentially generated during the cooling process of the molten pool. When the addition content of NbC increased to 15wt.%, the diffraction peak of Cr_7C_3 could not be observed in the

diffraction pattern, indicating that the relative content of each phase in the coating changed significantly with the increase in the content of NbC. The study of Khvan et al. (Ref 32) on the Fe-Cr-C ternary alloy system shows that the Gibbs free energy of $Cr_{23}C_6$ is lower than Cr_7C_3 when the temperature is below 1773 K, so it is observed that the diffraction peak of Cr_7C_3 disappears before that of $Cr_{23}C_6$ in the coating diffraction

pattern. The reaction equations to generate the corresponding free energy changes of Cr_7C_3 and $Cr_{23}C_6$ are as follows (Ref 33):

$$7Cr + 3C \rightarrow Cr_7C_3 \quad \text{(Eq 1)}$$

$$\Delta G^0 \left(KJ\ mol^{-1}\right) = -174.401 \\ - 0.0259T(298\ K < T < 2171\ K) \quad \text{(Eq 2)}$$

$$23Cr + 6C \rightarrow Cr_{23}C_6 \quad \text{(Eq 3)}$$

$$\Delta G^0 \left(KJ\ mol^{-1}\right) = -309.616 \\ - 0.0774T(298\ K < T < 1773\ K) \quad \text{(Eq 4)}$$

In order to understand the distribution of microstructure of the coatings, six sets of coatings were analyzed sequentially using body microscope and SEM. Figure 6 shows the macroscopic morphology of the coatings and the microstructure of the three regions of the coatings: upper, middle and bottom. As shown in Fig. 6(a)-(a3), the 1# coating is a continuous mesh structure. Observing Fig. 6(b)-(f), it is not difficult to notice that the mesh structure is fractured after the addition of NbC, and its microstructure is more uniform. The refinement and homogenization of the microstructure are most obvious when the NbC content is increased to 20 wt.%.

As shown in Fig. 7, in order to understand the distribution of NbC in the coatings, one region each in the upper, middle and bottom of the coatings was selected to take backscattered electron micrographs with a SEM. From the figure, it can be seen that the distribution of phases in the top, middle and bottom regions of the coating is similar, which proves that the generated coatings are uniform and stabilized. Figure 7(a1)-(a3) shows the microstructure and morphology of the three regions of the 1# coating, and it can be seen that the main phases are the matrix, the gray connected to the mesh structure and the irregularly shaped black phase, respectively. Figure 7(b1)-(f3) shows the microstructure and morphology of the selected areas in the top, middle and bottom of the 2#-6# coatings, respectively. It is noteworthy that the presence of bright white NbC phase was hardly observed in the microstructure of 2# coating. This may be due to the low incorporation of NbC and its predominance as a powder with nanoscale particle size, which was burned or not effectively introduced during the laser cladding process. Uniformly distributed white NbC phases can be seen in the backscattered images of the 3#-6# coatings, and the particle size of the generated NbC shows an increasing trend with the increase in the NbC design content.

To further evaluate the morphology of the generated carbides, the bright white NbC phase and the gray carbide phase in Fig. 7 were counted in terms of area share using Image Pro software. As shown in Table 5, with the increase in the design content of NbC, the area percentage of NbC in the coatings increased from 0.62% in 2# coatings to 7.13% in 6# coating, and the uniform distribution of NbC is favorable to improve the wear resistance of the coatings. However, the area share of the gray phase progressively decreases, and finally, the total carbide share decreases from 42.52% in 1# coating to 35.53% in 6# coating, which limits the further improvement of the microhardness of the coatings (Ref 32).

In addition, the morphology of NbC was characterized by Roundness with the following equation (Ref 34):

$$Roundness = L^2/(4\pi S) \quad \text{(Eq 5)}$$

where L is the perimeter of the white NbC particles and S is the area of the particles in the cross section. The bright white NbC phase in Fig. 7 was used as samples for statistics, and the results are shown in Fig. 8. It is found that with the increase in the NbC addition, the volume of NbC in the coating is larger and the complexity becomes higher. This is due to the fact that with the increase in the NbC addition, the content of Nb and C elements in the molten pool increases, which results in greater structural complexity at the corners of the bulk crystals by greater supercooling, obtaining a greater growth rate and gradually growing petallike NbC with different morphologies.

The coatings were face-scanned using the energy spectroscopy probe supplied within the SEM in order to analyze the elemental distribution. Figure 9 shows that elements such as Fe, Cr and Nb are dissolved in the matrix to form γ-Ni solid solution. The gray phase is mainly composed of Cr and C elements, and the major elements of the irregularly shaped black phase are Cr and B. Combined with XRD, it can be identified as $Cr_{23}C_6$ and Cr_2B, respectively.

Table 4 and Fig. 6 show that the addition of NbC has a refining effect on the grains in the coating. To further analyze this result, EBSD analysis was performed on the coating of samples #1 and #5. The results of EBSD analysis were processed with the help of channel 5 software. Figure 10 shows the statistical results of the average grain size of the 1# and 5# coatings near the surface layer. The average size of the grains of 5# coating is about 0.6 times of that of 1# coating.

As shown in Fig. 11, the kernel average misorientation (KAM) diagram is plotted using EBSD analysis software. The KAM diagram reflects the degree of plastic deformation in the selected region. The brighter the color, the higher the density of geometric dislocations and the more concentrated the stresses (Ref 35). It can be seen that the residual stress of the 5# coating with NbC addition is substantially higher, and the stress concentration near the carbide is more obvious. This is a shortcoming of the mechanical addition method for preparing composite coatings, where the cracking of the coating is more pronounced due to the mismatch between the thermal expansion coefficient and elastic modulus between the hard phase and the substrate.

3.2 Microhardness Analysis

The microhardness of the coating surface is shown in Fig. 12. The average microhardness of 1#, 2#, 3#, 4#, 5# and 6# coatings is 504.1 $HV_{0.2}$, 531.0 $HV_{0.2}$, 537.6 $HV_{0.2}$, 545.9 $HV_{0.2}$, 561.6 $HV_{0.2}$ and 534.9 $HV_{0.2}$, respectively. After the addition of NbC, the microhardness of the coating is slightly increased, and the 5# coating has the highest microhardness, which is 11.4% higher than that of the 1# coating, and about 2.13 times of the average microhardness of the substrate (266.7 $HV_{0.2}$). NbC decomposes under the high temperature of the melt pool and some of the carbon elements are burned off. The added NbC content in the coating did not reach the design composition, and the preferential generation of NbC during the cooling of the melt pool reduces the precipitation phase of $Cr_{23}C_6$ and Cr_7C_3, which have higher hardness in the coating, so the improvement of the coating microhardness is not obvious (Ref 36).
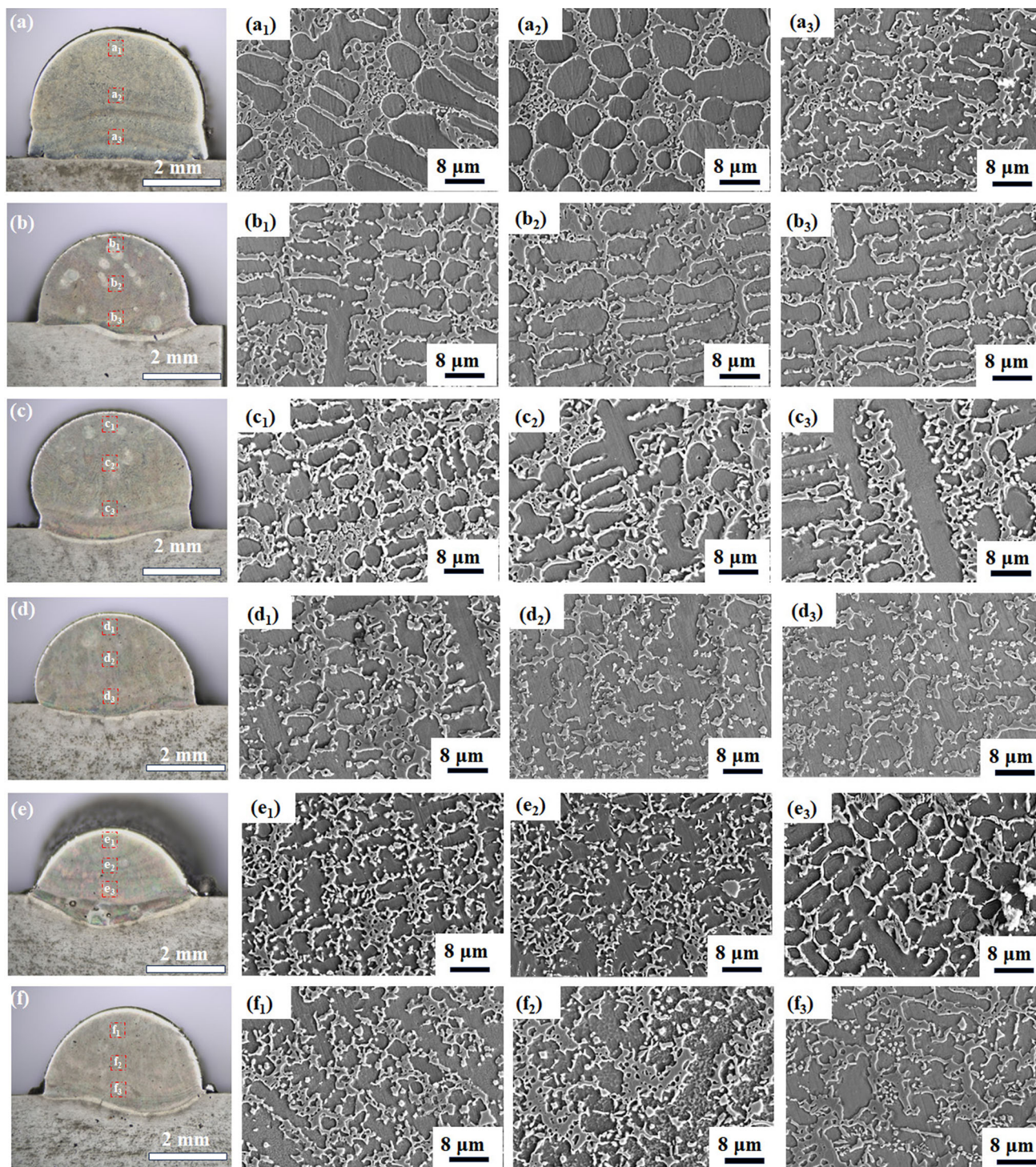
Fig. 6 Macroscopic morphology and microstructure morphology of the coatings: (a-f) macroscopic morphology of 1#-6# coatings under the body microscope; (a1-f3) microstructure pictures of the upper, middle and lower regions of 1#-6# coatings (SE)

3.3 Wear Resistance Analysis

The wear loss and wear resistance of the coatings after 2 h wear under 98 N and 196 N load are shown in Fig. 13. As shown in Fig. 13(a), after adding 15 wt.% and 25 wt.% NbC, the wear loss of the coating is reduced to 5.5 mg, and the wear resistance is the best, which is 1.66 times that of the 1# coating. As a whole, the wear resistance of the coating increases with the increase in the NbC content under 98 N load. Figure 13(b)

shows that after 2 h wear under 196 N load, the 1# coating wears up to 78.7 mg. After adding NbC, the wear loss of the coatings decreased significantly, which were 24.0, 22.0, 21.7, 16.9 and 20.2 mg, respectively. The reciprocal of wear rate was used to represent the wear resistance of the coating, which firstly increased and then decreased with the increase in the NbC addition. The wear resistance of the 5# coating is the best, reaching 7.10 min/mg, which is 4.66 times that of the 1#
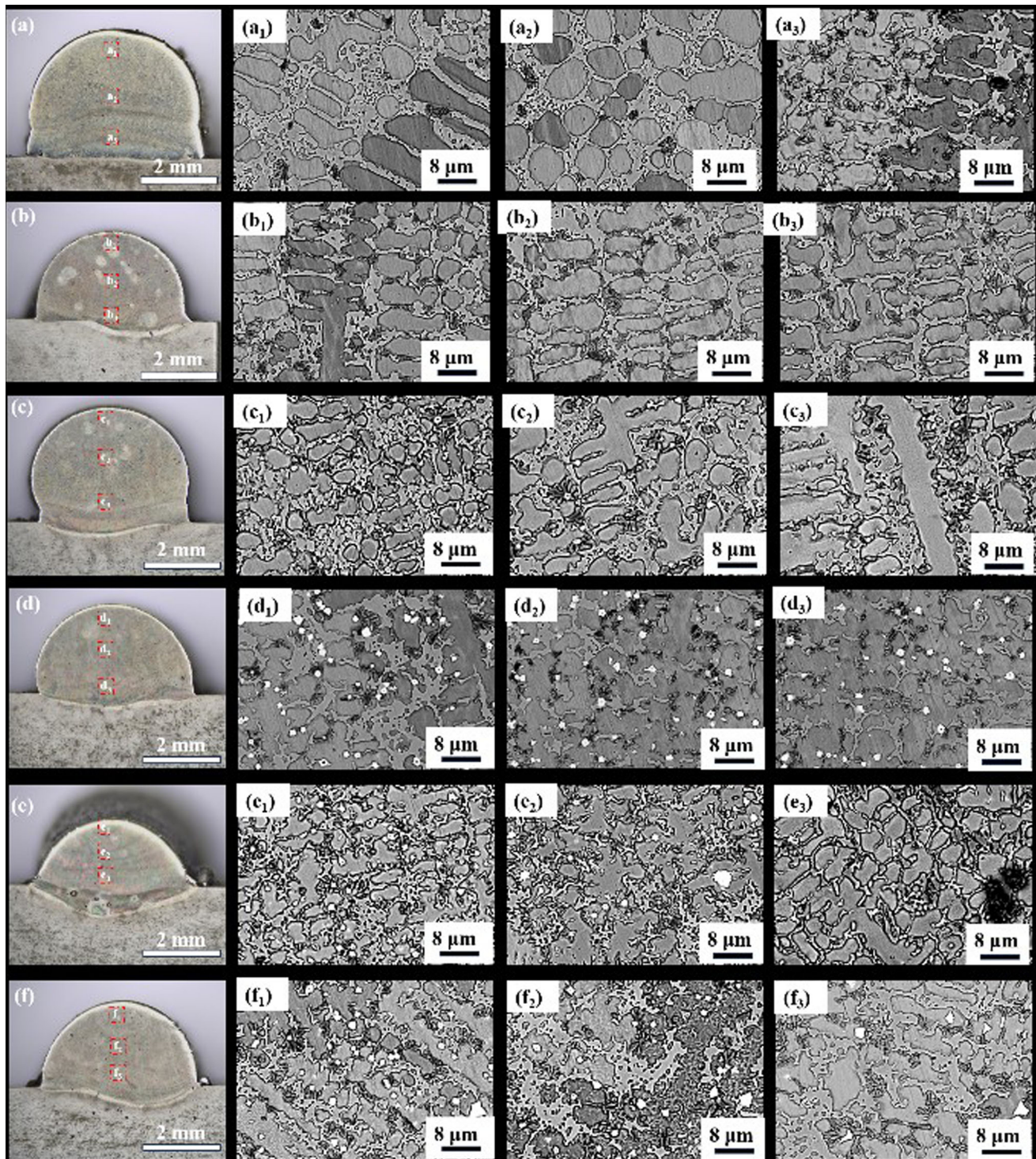
Fig. 7 Macroscopic morphology and microstructure morphology of the coatings: (a-f) macroscopic morphology of 1#-6# coatings under the body microscope; (a1-f3) microstructure pictures of the upper, middle and lower regions of 1#-6# coatings (BSE)

coating. The wear resistance of coatings under two loads is slightly different. This is mainly due to the increase in the load, the contact area between the grinding ring and the sample increases, and the protrusions of the grinding ring are more deeply embedded in the coating, causing more material surface shedding. Therefore, the improvement of the wear resistance of the 5# coating under higher loads may be due to the stronger bond between the ceramic phase and the matrix (Ref 37). The

addition of NbC enhances the wear resistance of the coating due to the fact that the addition of NbC promotes the homogeneity of the coating microstructure and reduces the size of the grains (Ref 38). However, as mentioned earlier, the hardness of the coating decreased after the increase in the NbC to 20 wt.% due to the burnout of the carbon element by the high temperature of the melt pool. This limits the further improvement of the wear resistance of the coating, and

therefore, the wear resistance of the 6# coating starts to decrease (Ref 39).

The friction coefficient of the coating is the ratio of the friction force of the coating subjected to the grinding ring to the load in the vertical direction. The lower the coefficient of friction, the better the wear resistance of the coatings. Figure 14 shows the time variation curve of the friction coefficient of each coating under 196 N load. The initial sample and the grinding ring are in the running-in period, and the friction coefficient gradually decreases with time and enters the stable wear stage after about 1000 s, and the friction coefficient fluctuates periodically around a certain value. From the point of view of average friction coefficient, the 1# coating has the highest average friction coefficient ($\mu_{1\#} = 0.434$), and the coating has the worst ability to reduce wear. After adding different content of NbC, the friction coefficient of the coatings decreases to different degrees, which are 0.138, 0.259, 0.256, 0.117 and 0.143, respectively. The average friction coefficient of the 5# coating decreases most obviously, which is only 26.96% of the 1# coating. The effect of the addition of NbC on the friction

coefficient of the coating is generally consistent with that on the wear resistance (Ref 40).

Figure 15(a)-(f), respectively, shows the three-dimensional contour reconstruction of the 1#-6# coating worn surface under laser confocal microscope and the section curve of the wear surface. The wear sag of the 1# coating is deeper, and the depth of the wear sag of the coating decreases dramatically when NbC is added, and the section curve tends to be gentle.

Figure 16 shows the wear morphology of the coating surface after friction and wear test of different components under 196 N load. Under scanning electron microscopy, different amounts of debris and grooves of different depths can be observed. As shown in Figs. 16(a) and 15(b), lamellar abrasive debris stick to the worn surface. This is due to the fact that the contact area between the grinding ring and the coating is subjected to vertical pressure and plastic deformation under the action of horizontal friction to form an adhesive contact. The contact grows and is shear in the process of moving along the horizontal direction, and finally, lamellar abrasive debris is formed on the surface of the coating under the action of vertical load. Therefore, the main wear mechanism of 1# and 2# coatings is adhesive wear. By comparing the wear morphologies of the two coatings, it is not difficult to find that the size of lamellar abrasive debris adhering to the surface of the 1# coating is larger and the adhesive wear is more serious, which indicates that 5wt.% NbC can also boost the wear resistance of the nickel-based coating.

Figure 16(c), 15(d) and 15(e), respectively, shows the wear morphologies of the 3#, 4# and 5# coatings. The evenly distributed NbC phase in the coating supports and protects the substrate during the wear process to avoid serious wear of

Table 5 Average area proportion of carbide in the SEM picture of the coating in Fig. 7 (%)

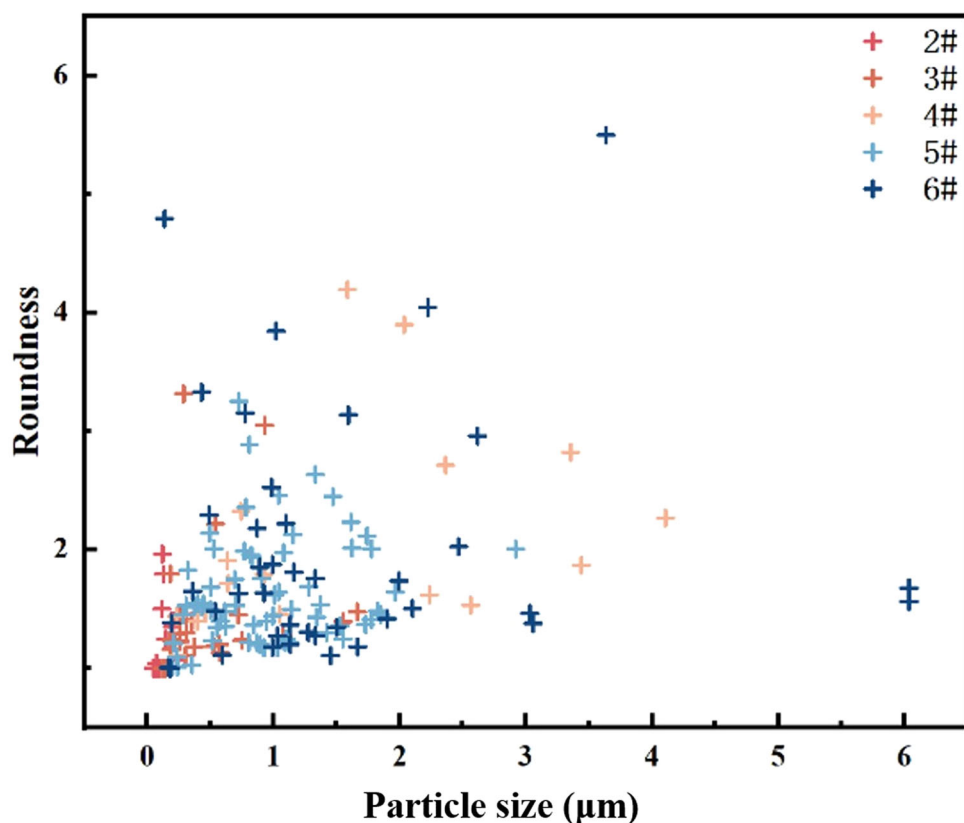|	1#	2#	3#	4#	5#	6#
NbC	0	0.62	3.85	4.57	6.96	7.13
Gray phase	42.52	40.48	34.49	32.63	27.86	27.40
Total	42.52	41.10	38.34	37.20	35.82	35.53

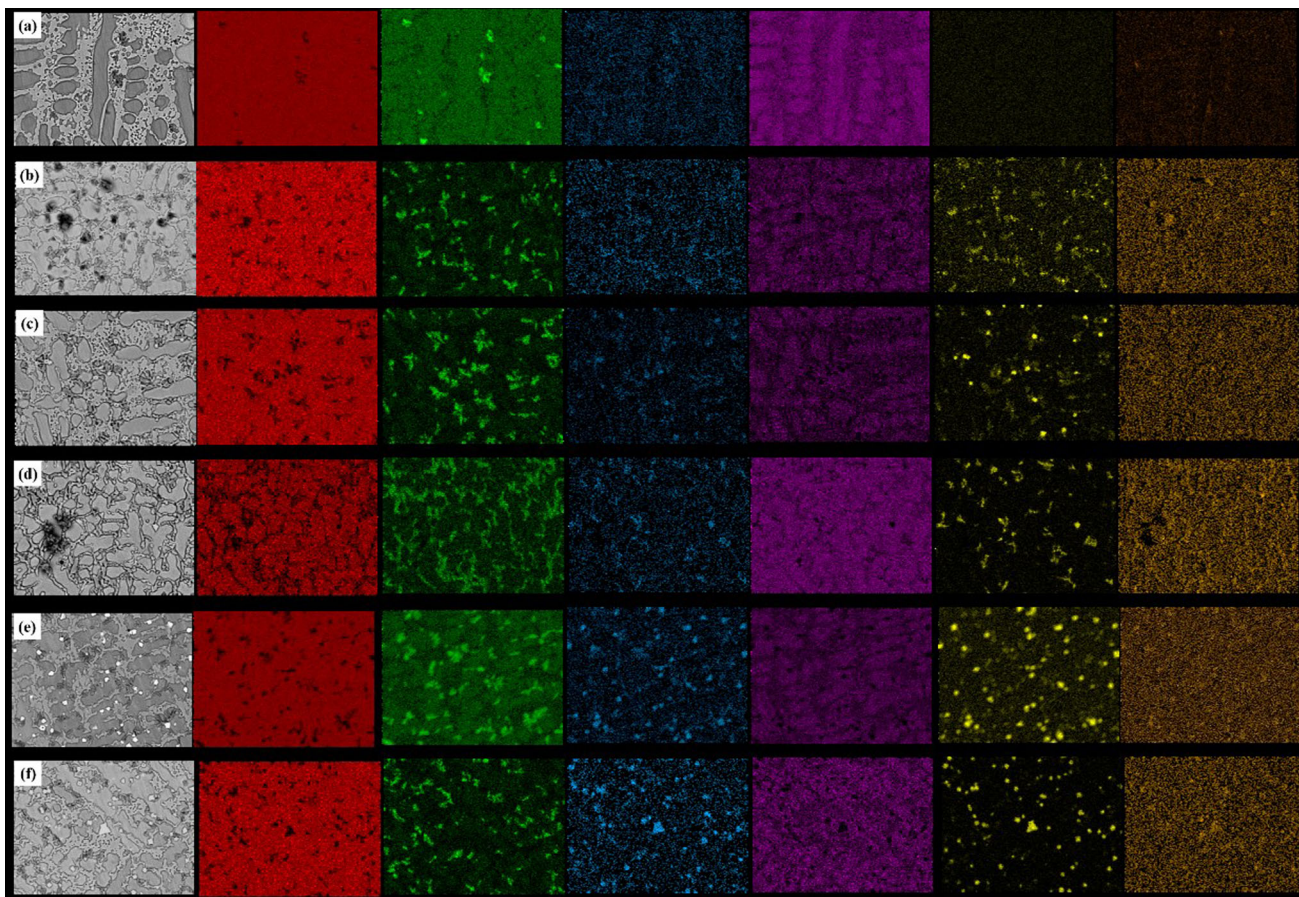Fig. 8 Roundness distribution of NbC particles in coatings

Fig. 9 Mapping scanning results of the coatings: (a) 1#; (b) 2#; (c) 3#; (d) 4#; (e) 5#; (f) 6#
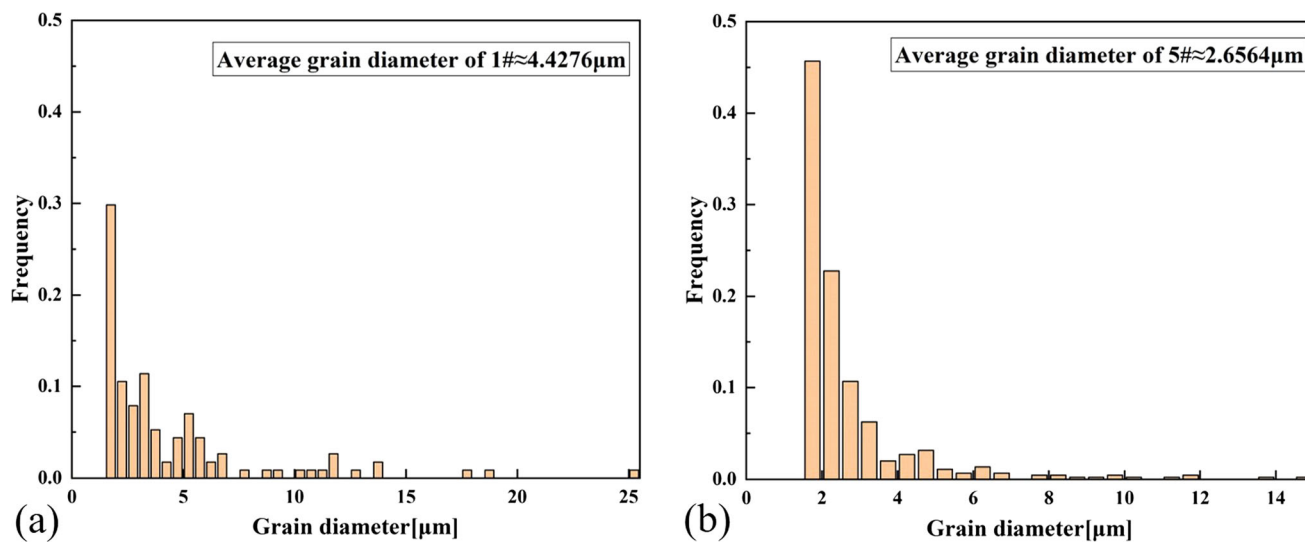

Fig. 10 Grain size statistics in the surface area of 1#(a) and 5#(b) laser clad coatings

abrasive particles on the substrate. There are a certain amount of debris and shallow grooves on the worn surface, so the wear mechanism of these three coatings is adhesive wear and abrasive wear. Moreover, it is not difficult to see that the number of debris on the surface of 5# coating is less and the average size is smaller. Figure 16(f) shows the worn surface of the 6# coating. As with the 5# coating, there are fewer debris on

the surface of the component coating, but there are significant grooves on the worn surface. This is due to the surface material migration of the coating under the action of hard phase or convex adhesion on the surface of the grinding ring. Therefore, the main wear mechanism of 6# coating is abrasive wear. EDS point analysis was performed on the selected debris in Fig. 16(e), and the mass fraction and atomic percentage of
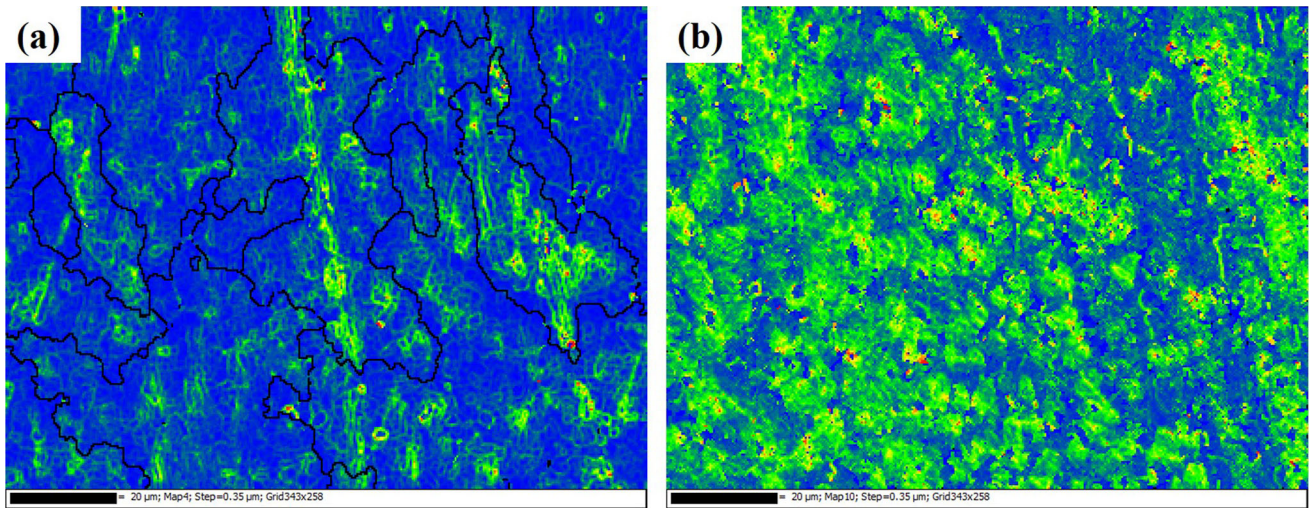
Fig. 11 KAM distribution of 1# (a) and 5# (b) laser cladding coatings
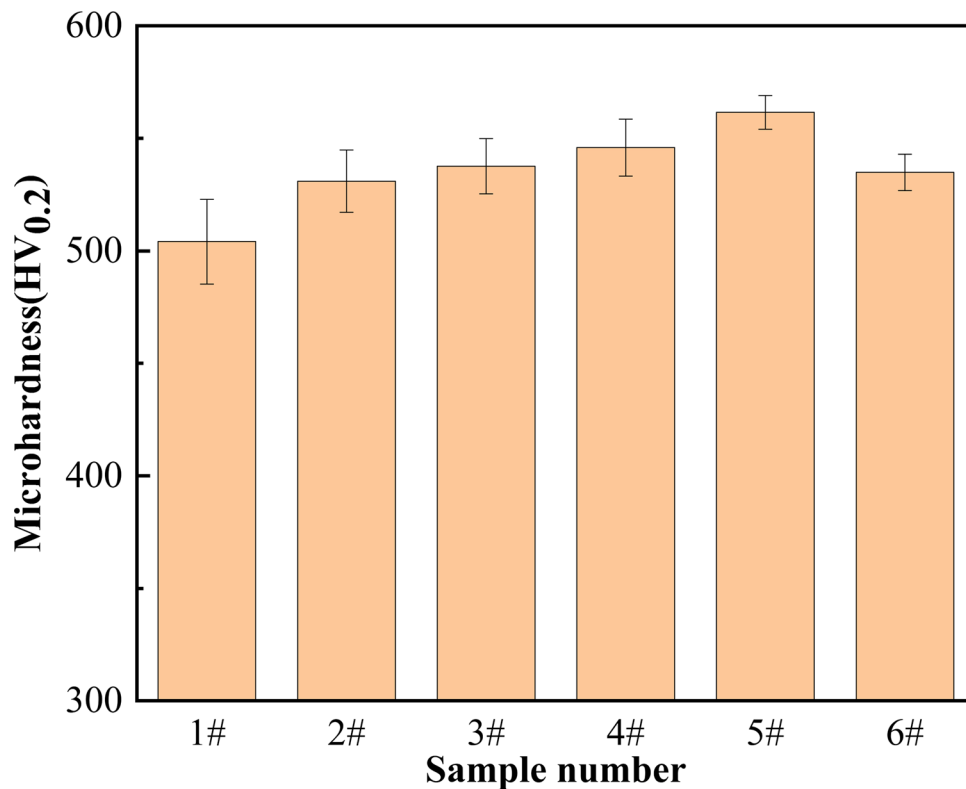

Fig. 12 Surface microhardness of coating

each element in the debris are shown in Table 6: The debris were dominated by O and Fe elements, indicating that wear occurred in the grinding ring during the test. Some materials were transferred to the coating surface for serious oxidation (Ref 41-43).

In order to further understand the distribution of elements on the wear surface of coating, EDS was used to scan the 5# wear surface. The mapping scanning results and the element mass fraction and atomic percentage are shown in Fig. 17 and Table 7. It can be seen that the main elements of the debris are Fe and O, and the material of the grinding ring is transferred to the surface of the coating in the process of friction and wear to

form the debris. Large amounts of Ni were detected in areas of the coating that were not covered by debris. In addition, uniformly distributed Cr and Nb were detected, which may be from the hard ceramic phases NbC, Cr23C6 and Cr7C3.

4. Conclusions

Ni45/NbC laser cladding composite coatings were prepared by direct addition method. The effect of NbC on the microstructure evolution and wear resistance of the coatings
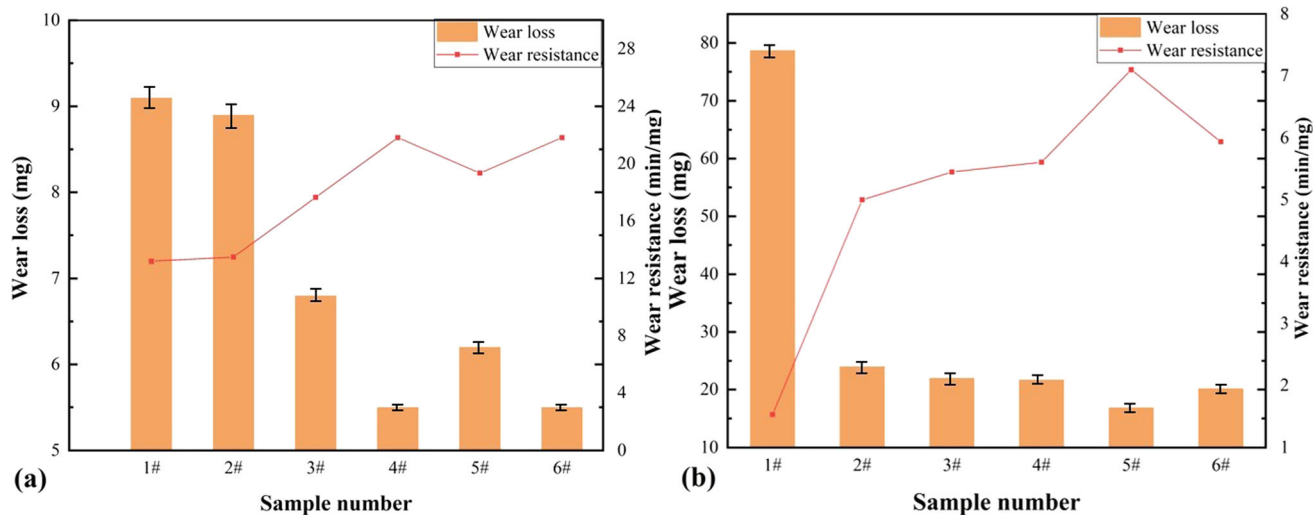
Fig. 13 Wear loss and wear resistance of the coating under 98 N load (a) and 196 N load (b)
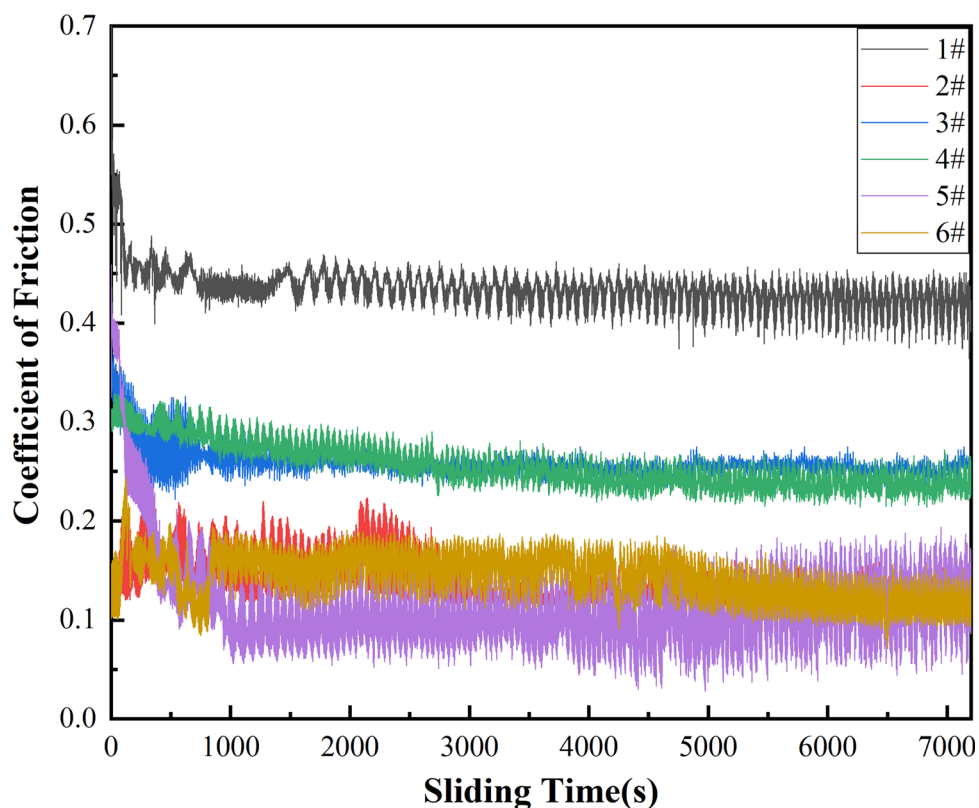

Fig. 14 Friction coefficient of the coating under 196 N load

was investigated by observing the microstructure and testing the microhardness and wear resistance, and the following conclusions could be drawn:

(1) The addition of micro- and nano-sized NbC has a certain effect on the enhancement of the coating microhardness, and the microhardness of the coating of #5 is most

obviously enhanced, which is about 112.0% of that of the specimen of 1# and about 2.13 times of the average microhardness of the substrate (266.7 $HV_{0.2}$). The NbC powder with nanoscale particle size suffered from burn-out during the laser cladding process, resulting in less than expected NbC content generated within the coatings. And due to the reduction in the $Cr_{23}C_6$ content,
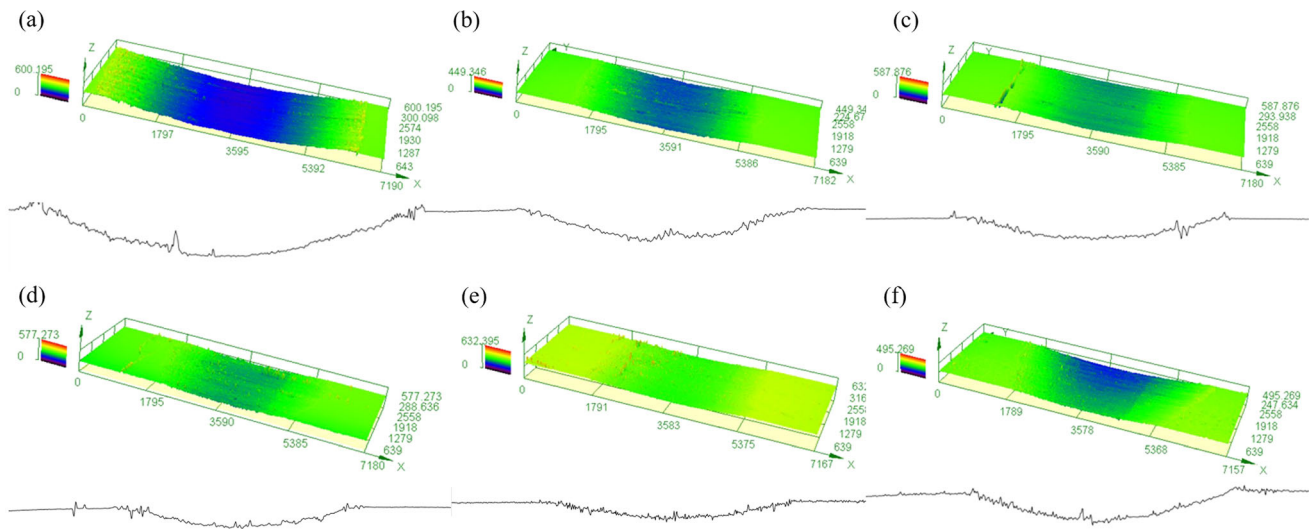
Fig. 15 Wear morphology of coating and cross-sectional curve of worn surface under laser confocal microscope: (a) 1#; (b) 2#; (c) 3#; (d) 4#; (e) 5#; (f) 6#
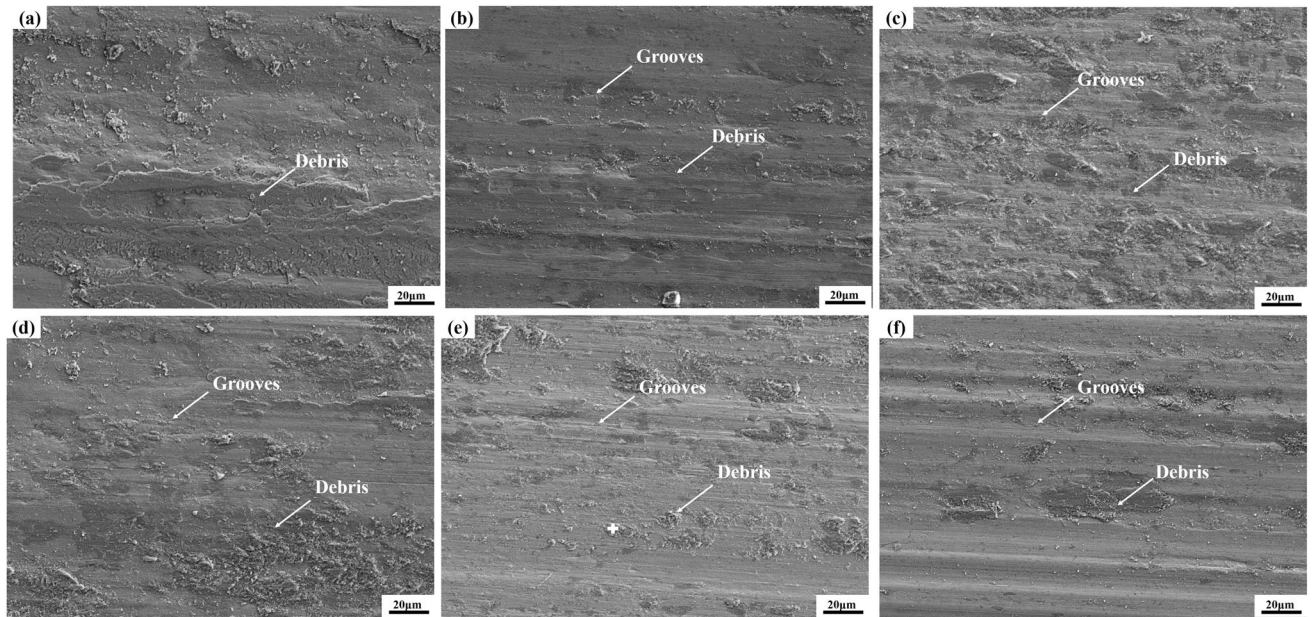

Fig. 16 Wear morphologies of different coating surfaces: (a) 1#; (b) 2#; (c) 3#; (d) 4#; (e) 5#; (f) 6#

Table 6 Mass fraction and atomic percentage of each element in the debris

Element	B	O	Si	Cr	Fe	Ni	Nb
wt.%	2.62	28.56	0.41	2.04	55.56	9.35	1.46
at.%	7.46	54.90	0.45	1.21	30.60	4.90	0.48

the total carbide content within the coating decreased from 42.52 to 35.53%, which limited the further improvement of the microhardness of the coatings.

(2) The microstructure of the coatings was refined due to the refinement around Nb. The dendrite arm spacing were all effectively reduced compared to 1# coating, and the 6# coating showed the best refinement effect, reduced to 64.7%. EBSD analysis showed that the grain size of 5# coating was reduced to 60% compared to 1# coating.

(3) The 4# and 6# coatings showed the best wear resistance at 98 N load, which were about 166.0% of that of the 1# coating. 5# coating showed the best wear resistance at 196 N load, which was about 466.0% of that of the 1# coating. The favorable wear resistance depends on the relatively high microhardness of the coatings and the uniformly distributed hard phase, which avoids spalling and fracture of the hard phase during frictional wear.
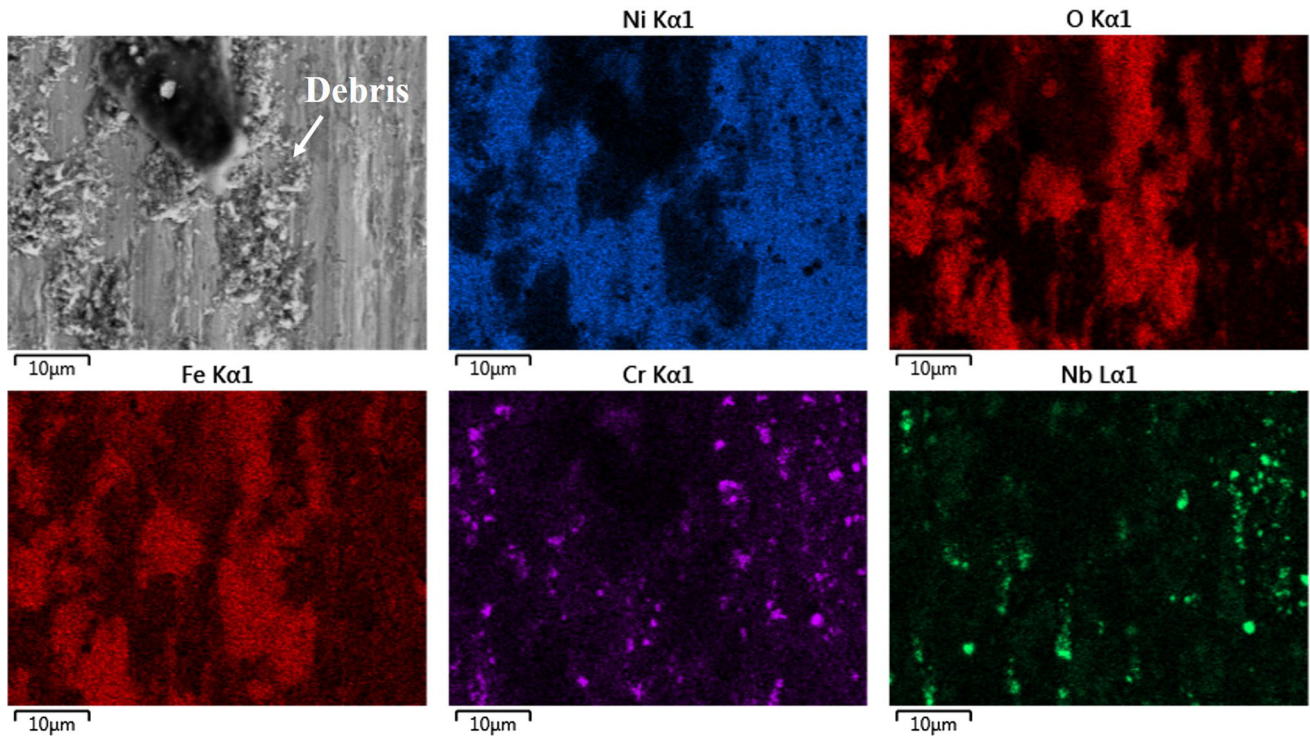
Fig. 17 EDS mapping scanning result of microstructure on 5# coating wear surface

Table 7 Mass fraction and atomic percentage of each element on 5# coating wear surface

Element	B	O	Si	Cr	Fe	Ni	Nb
wt.%	0.3	11.38	2.23	6.17	23.04	53.35	3.42
at.%	0.35	31.21	3.49	5.21	18.11	38.89	1.61

References

1. Z. Liu, J.H. Lu, and P. Zhu, Lightweight Design of Automotive Composite Bumper System Using Modified Particle Swarm Optimizer, *Compos. Struct.*, 2016, **140**, p 630–643
2. B. Zeng, H. Li, C.W. Mao, and Y. Wu, Modeling, Prediction and Analysis of New Energy Vehicle Sales in China Using a Variable-Structure Grey Model, *Expert Syst. Appl.*, 2022, **213**, p 118879
3. J.B. Hao, F.T. Hu, X.W. Le, H. Liu, H.F. Yang, and J. Han, Microstructure and High-Temperature Wear Behaviour of Inconel 625 Multi-layer Cladding Prepared on H13 Mould Steel by a Hybrid Additive Manufacturing Method, *J. Mater. Process. Technol.*, 2021, **291**, p 117036
4. W. Zhao, G.C. Zha, F.X. Kong, M.L. Wu, X. Feng, and S.Y. Gao, Strengthening Effect of Incremental Shear Deformation on Ti Alloy Clad Plate with a Ni-Based Alloy Laser-Clad Layer, *J. Mater. Eng. Perform.*, 2017, **26**(5), p 2411–2416
5. P.C. Priarone, G. Campatelli, A.R. Catalano, and F. Baffa, Life-Cycle Energy and Carbon Saving Potential of Wire Arc Additive Manufacturing for the Repair of Mold Inserts, *J. Mater. Sci. Technol.*, 2021, **35**, p 943–958
6. C.M. Sample, V.K. Champagne, A.T. Nardi, and D.A. Lados, Factors Governing Static Properties and Fatigue, Fatigue Crack Growth, and Fracture Mechanisms in Cold Spray Alloys and Coatings/Repairs: A Review, *Addit. Manuf.*, 2020, **36**, p 101371
7. M. Ragavendran, M. Vasudevan, and H. Hussain, Study of the Microstructure, Mechanical Properties, Residual Stresses, and Distortion in Type 316LN Stainless Steel Medium Thickness Plate Weld Joints, *J. Mater. Eng. Perform.*, 2022, **31**(6), p 5013–5025
8. K.M. Wang, B.H. Chang, J.S. Chen, H.G. Fu, Y.H. Lin, and Y.P. Lei, Effect of Molybdenum on the Microstructures and Properties of Stainless Steel Coatings by Laser Cladding, *Appl. Sci.*, 2017, **7**(10), p 1065. https://doi.org/10.3390/app7101065
9. S.T. Sun, H.F. Han, X.L. Ping, X.Y. Guo, J. Lin, Y.P. Lei, W.B. Wu, and J.X. Zhou, Effect of Liquid Nitrogen Cooling on Grain Growth and Properties of Laser Cladding In-Situ (Ti, Nb) C/Ni Composite Coatings, *Mater. Charact.*, 2019, **152**, p 115–129
10. C.P. Paul, B.K. Gandhi, P. Bhargava, D.K. Dwivedi, and L.M. Kukreja, Cobalt-Free Laser Cladding on AISI Type 316L Stainless Steel for Improved Cavitation and Slurry Erosion Wear Behavior, *J. Mater. Eng. Perform.*, 2014, **23**(12), p 4463–4471
11. Z.T. Gao, H.B. Ren, H.M. Geng, Y. Yu, Z.M. Gao, and C.W. Zhang, Effect of CeO_2 on Microstructure and Wear Property of Laser Cladding Ni-Based Coatings Fabricated on 35CrMoV Steel, *J. Mater. Eng. Perform.*, 2022, **31**(11), p 9534–9543
12. Y.L. Gao, Y. Tong, G.H. Li, P. Lu, and D. Zhang, Microstructure and Mechanical Properties of Ni-Based Alloy Composite Coating on Cr12MoV by Laser Cladding, *Coatings*, 2022, **12**(11), p 1632. https://doi.org/10.3390/coatings12111632
13. H.G. Yin, J.H. Li, L.W. Zhao, and F.P. Yao, Simulation of in-Situ Preheating of Ni-Based Multi-Layer and Multi-pass Coatings on H13 Steel, *J. Mech. Sci. Technol.*, 2022, **36**, p 4671–4680
14. R.F. Di, J.Q. Zhang, Q. Zhu, F. Yan, H.F. Tian, H.Y. Song, and J.B. Lei, Effect of WC-12Co on the Mechanical and Wear Performance of Laser Melting Deposition Nickel-Based Alloy, *Opt. Laser Technol.*, 2022, **152**, p 108094. https://doi.org/10.1016/j.optlastec.2022.108094
15. L.Y. Chen, T.B. Yu, X. Chen, Y. Zhao, and C. Guan, Process Optimization, Microstructure and Microhardness of Coaxial Laser Cladding TiC Reinforced Ni-Based Composite Coatings, *Opt. Laser Technol.*, 2022, **152**, p 108129. https://doi.org/10.1016/j.optlastec.2022.108129

16. Y.T. Li, H.G. Fu, T.J. Ma, K.M. Wang, X.J. Yang, and J. Lin, Microstructure and Wear Resistance of AlCoCrFeNi-WC/TiC Composite Coating by Laser Cladding, *Mater. Charact.*, 2022, **194**, p 112479. https://doi.org/10.1016/j.matchar.2022.112479

17. Y. Zhao, T.B. Yu, J.Y. Sun, and S.X. Jiang, Microstructure and Properties of Laser Cladded B4C/TiC/Ni-Based Composite Coating, *Int. J. Refract. Met. Hard Mater*, 2020, **86**, p 105112. https://doi.org/10.1016/j.ijrmhm.2019.105112

18. J.Y. Zeng, G.F. Lian, C.R. Chen, and H. Xu, Influences of the TiC Composite Introduction Method on the Microstructures and Properties of Nickel-Based Coatings, *Opt. Laser Technol.*, 2022, **156**, p 108633. https://doi.org/10.1016/j.optlastec.2022.108633

19. J.D. Majumdar, S.K. Rittinghaus, K. Wissenbach, D. Hoeche, C. Blawert, and A. Weisheit, Microstructural Evolution and Microhardness of Direct Laser Clad TiC Dispersed Titanium Aluminide (Ti$_{45}$Al$_5$Nb$_{0.5}$Si) Alloy, *Proc. Manuf.*, 2019, **35**, p 840–846

20. H. Zhang, Y.J. Pan, Y. Zhang, G.F. Lian, Q. Cao, and J.H. Yang, Influence of Laser Power on the Microstructure and Properties of In-Situ NbC/WCoB–TiC Coating by Laser Cladding, *Mater. Chem. Phys.*, 2022, **290**, p 126636. https://doi.org/10.1016/j.matchemphys.2022.126636

21. Y. Zhao, L.Y. Chen, J.Y. Sun, W.Z. Wu, and T.B. Yu, Microstructure Evolution and Wear Resistance of In-Situ Synthesized (Ti, Nb)C Ceramic Reinforced Ni$_2$0$_4$ Composite Coatings, *Ceram. Int.*, 2022, **48**(12), p 17518–17528

22. X.F. Li, X.H. Yang, D.H. Yi, B.S. Liu, J.C. Zhu, J.X. Li, C. Gao, and L.Z. Wang, Effects of NbC Content on Microstructural Evolution and Mechanical Properties of Laser Cladded Fe$_{50}$Mn$_{30}$Co$_{10}$Cr$_{10}$-xNbC Composite Coatings, *Intermetallics*, 2021, **138**, p 107309. https://doi.org/10.1016/j.intermet.2021.107309

23. L.Y. Chen, T.B. Yu, P.F. Xu, and B. Zhang, In-Situ NbC Reinforced Fe-Based Coating by Laser Cladding: Simulation and Experiment, *Surf. Coat. Technol.*, 2021, **412**, p 127027. https://doi.org/10.1016/j.surfcoat.2021.127027

24. K.M. Wang, D. During, G. Lian, B.H. Chang, J. Ju, S.T. Sun, and H.G. Fu, Microstructure and Property of Laser Clad Fe-Based Composite Layer Containing Nb and B4C Powders, *J. Alloys Compd.*, 2019, **802**, p 373–384

25. Y.B. Cao, S.X. Zhi, H.B. Qi, Y. Zhang, C. Qin, and S.P. Yang, Evolution Behavior of Ex-Situ NbC and Properties of Fe-Based Laser Clad Coating, *Opt. Laser Technol.*, 2020, **124**, p 105999. https://doi.org/10.1016/j.optlastec.2019.105999

26. Y.P. Liu, K.M. Wang, H.G. Fu, B. Zong, and J.G. Zhang, Wear Resistance of In Situ NbC - Reinforced Laser Cladding Ni45 Coatings, *Lubricants*, 2023 https://doi.org/10.3390/lubricants11080316

27. R. Casati and M. Vedani, Metal Matrix Composites Reinforced by Nano-Particles-A Review, *Metals*, 2014, **4**, p 64–81

28. S.T. Sun, H.G. Fu, X.L. Ping, X.Y. Guo, J. Lin, Y.P. Lei, W.B. Wu, and J.X. Zhou, Formation Mechanism and Mechanical Properties of Titanium-Doped NbC Reinforced Ni-Based Composite Coatings, *Appl. Surf. Sci.*, 2019, **476**, p 914–927

29. Q.Y. Wang, Y.C. Xi, X.Y. Liu, S. Liu, S.L. Bai, and Z.D. Liu, Microstructure and Mechanical Properties of Interface Between Laser Cladded Hastelloy Coating and Steel Substrate, *Trans. Nonferr. Metals Soc. China*, 2017, **27**(3), p 733–740

30. Z. Ma, C. Xia, H. Zhong, T. Yang, N. Liu, C. Liang, and Q. Li, Microstructure, Mechanical Property and Corrosion Resistance of FeCoCrNi-M High-Entropy Alloy Coatings on 6061 Aluminum Alloy Prepared by Laser Cladding, *Surf. Coat. Technol.*, 2023, **455**, p 129217. https://doi.org/10.1016/j.surfcoat.2022.129217

31. G. Dong, B. Yan, Q.L. Deng, and T. Yu, Microstructure and Wear Resistance of in situ NbC Particles Reinforced Ni-based Alloy Composite Coating by Laser Cladding, *J. Wuhan Univ. Technol. Mater.*, 2012, **27**, p 231–237

32. A.V. Khvan, B. Hallstedt, and C. Broeckmann, A Thermodynamic Evaluation of the Fe–Cr–C System, *Calphad*, 2014, **46**, p 24–33

33. Q.L. Wu, W.G. Li, N. Zhong, W. Gang, and H.S. Wang, Microstructure and Wear Behavior of Laser Cladding VC-Cr$_7$C$_3$ Ceramic Coating on Steel Substrate, *Mater. Des.*, 2013, **49**, p 10–18

34. Q.S. Ma, Y.J. Li, and J. Wang, Effects of Ti Addition on Microstructure Homogenization and Wear Resistance of Wide-Band Laser Clad Ni60/WC Composite Coatings, *Int. J. Refract. Met. Hard Mater*, 2017, **64**, p 225–233

35. P.C. Jiang, R.F. Li, Y. Zhao, X.Q. Zhang, and P.L. Zhang, Effect of Rotating Magnetic Field on Microstructure and Tribological Properties of Laser Cladded Nickel-Based Coatings, *J. Mater. Res. Technol.*, 2023, **24**, p 1335–1343

36. S.L.Z. Hong, Q.S. Ma, G. Liu, H. Yang, L. Hu, W. Meng, and H, Xie and X. H, Yin, In-Situ Reinforced Phase Evolution and Wear Resistance of Nickel-Based Composite Coatings Fabricated by Wide-Band Laser Cladding with Nb Addition, *Opt. Laser Technol.*, 2023, **157**, p 108678. https://doi.org/10.1016/j.optlastec.2022.108678

37. P. Bagde, S.G. Sapate, R.K. Khatirkar, and N. Vashishtha, Friction and Abrasive Wear Behaviour of Al$_2$O$_3$-13TiO$_2$ and Al$_2$O$_3$-13TiO$_2$+Ni Graphite coatings, *Tribol. Int.*, 2018, **121**, p 353–372

38. J.Q. Hu, H.X. Song, S. Sandfeld, X.M. Liu, and Y.G. Wei, Breakdown of Archard Law Due to Transition of Wear Mechanism from Plasticity to Fracture, *Tribol. Int.*, 2022, **173**, p 107660. https://doi.org/10.1016/j.triboint.2022.107660

39. Q.T. Li, Y.P. Lei, and H.G. Fu, Growth Mechanism, Distribution Characteristics and Reinforcing Behavior of (Ti, Nb)C Particle in Laser Cladded Fe-Based Composite Coating, *Appl. Surf. Sci.*, 2014, **316**, p 610–616

40. F. Findik, Latest Progress on Tribological Properties of Industrial Materials, *Mater. Des.*, 2014, **57**, p 218–244

41. J. Li, Z. Liu, H. Ma, Q. Liu, J. Mao, J. Zhang, and Y. Kong, Comparative Study on the Corrosion Behaviour of 1.4529 Super Austenitic Stainless Steel and Laser-Cladding 1.4529 Coating in Simulated Desulfurized Flue Gas Condensates, *Corros. Sci.*, 2022, **209**, p 110794. https://doi.org/10.1016/j.corsci.2022.110794

42. A. Pizzatto, M.F. Teixeira, A. Rabelo, T. Falcade, and A. Scheid, Microstructure and Wear Behavior of NbC-Reinforced Ni-Based Alloy Composite Coatings by Laser Cladding, *Mater. Res. Am. J. Mater.*, 2021, **24**(3), p e20200447. https://doi.org/10.1590/1980-5373-MR-2020-0447

43. Z.X. Zhu, X.B. Liu, Y.F. Liu, S.Y. Zhang, M. Yuan, H.B. Zhou, and S.H. Zhang, Effects of Cu/Si on the Microstructure and Tribological Properties of FeCoCrNi High Entropy Alloy Coating by Laser Cladding, *Wear*, 2023, **512**, p 204533. https://doi.org/10.1016/j.wear.2022.204533